Three-dimensional bulk Fermi surfaces and Weyl crossings of Co_2MnGa thin films underneath a protection layer

Takashi Kono,[1] Masaaki Kakoki,[1] Tomoki Yoshikawa,[1] Xiaoxiao Wang,[1] Kazuki Sumida,[2] Takayuki Muro,[3] Kazuki Goto,[4] Yuya Sakuraba,[4,5] Rie Y. Umetsu,[6,7,8] and Akio Kimura[1,9,*]

[1]*Department of Physical Sciences, Graduate School of Science, Hiroshima University, 1-3-1 Kagamiyama, Higashi-hiroshima 739-8526, Japan*

[2]*Materials Sciences Research Center, Japan Atomic Energy Agency, Hyogo 679-5148, Japan*

[3]*Japan Synchrotron Radiation Research Institute (JASRI), 1-1-1 Kouto, Sayo, Hyogo 679-5198, Japan*

[4]*National Institute for Materials Science, 1-2-1 Sengen, Tsukuba 305-0047, Japan*

[5]*PRESTO, Japan Science and Technology Agency, Saitama 332-0012, Japan*

[6]*Institute for Materials Research, Tohoku University, 2-1-1 Katahira, Aoba-ku, Sendai 980-8577, Japan*

[7]*Center for Spintronics Research Network, Tohoku University, 2-1-1 Katahira, Sendai 980-8577, Japan*

[8]*Center for Science and Innovation in Spintronics, Tohoku University, 2-1-1 Katahira, Aoba-ku, Sendai 980-8577, Japan*

[9]*Graduate School of Advanced Science and Engineering, Hiroshima University, 1-3-1 Kagamiyama, Higashi-hiroshima 739-8526, Japan*

(Received 6 August 2021; accepted 20 October 2021; published 8 November 2021)

Angle-resolved photoelectron spectroscopy utilizing soft x-ray synchrotron radiation was applied to Heusler-type Co_2MnGa thin films that have a 1-nm Al capping layer. The bulk Fermi surfaces and band structures varied along the out-of-plane momentum, stemming from the three-dimensional crystal structure, in the absence of any *in situ* surface treatment. In addition, there were characteristic intersecting bands (Weyl cones), with crossing points near the Fermi level, which were consistent with computed results. The Weyl cones are of bulk origin and are responsible for the high anomalous Nernst and the anomalous Hall coefficients. A close comparison of the experimental band structures in Co_2MnGe and Co_2MnGa indicated that the rigid band picture is valid in both alloys and that fine carrier tuning is possible by replacing Ga with Ge to improve the anomalous conductivity.

DOI: 10.1103/PhysRevB.104.195112

I. INTRODUCTION

Thermoelectric conversion of heat into electricity is a key technology for self-sustaining power sources for various sensors in the Internet of Things. So far, the conversion has been based on the Seebeck effect, which generates an electric field in a direction parallel to the heat flow. Widely used Seebeck devices have complex structures of multiple columns of thermoelectric materials connected in series. In the anomalous Nernst effect (ANE), the propagation direction of the carriers is curved by the magnetization of the material, resulting in an electric field in the direction perpendicular to both the magnetization and the heat flow. This simplifies device structures and enables thermoelectric generation over a large area. However, the small thermopower must be increased for widespread thermoelectric applications.

Recently, the Nernst thermopower exhibited a record maximum of 6–8 μV/K for the bulk Co_2MnGa crystals [1–3]. This was two orders of magnitude larger than those of conventional pure transition metals, and the substantial ANE was attributed to the presence of Weyl fermions that induce an emergent magnetic flux (Berry curvature) in the band structure [4–6]. The bulk crystal does not exhibit ANE in the absence of the external field because of a small magnetocrystalline anisotropy that causes multiple magnetic domains. Therefore, the bulk crystal is not suited for practical applications. However, a recent effort to transfer this function into the Co_2MnGa thin films overcame this problem and a carrier-tuned film exhibited a maximum thermopower of 6.2 μV/K. This was comparable to that of the bulk crystal, but with full remanent magnetization [7,8]. In addition, transverse thermoelectric generation was recently proposed using Co_2MnGa/Si hybrid materials, where the Si-produced longitudinal thermoelectric current generated a transverse electric field via a large anomalous Hall effect (AHE) in the Co_2MnGa thin film [9].

To gain insight into the driving forces of the large ANE and AHE, experimental determinations of three-dimensional band structures and Fermi surfaces are critical. The Hall coefficient is generally determined by the shape of the Fermi surfaces, and photoelectron spectroscopy is a powerful way to investigate electronic structures in materials [10]. To date, the photoelectron spectroscopy has been used to characterize bulk crystals [11–16] and thin films [7,17–32] of Co_2Mn-based full-Heusler alloys. In particular, earlier spectra for thin-film Co_2MnGa were acquired in an angle-integrated mode. However, specific information on band dispersions and three-dimensional Fermi surfaces were missing [20,22]. Recent angle-resolved photoelectron spectroscopy (ARPES) experiments via laser excitation revealed a feature near the Brillouin zone center, but were unable to access Weyl fermions located far away from the zone center because of the low excitation

*akiok@hiroshima-u.ac.jp

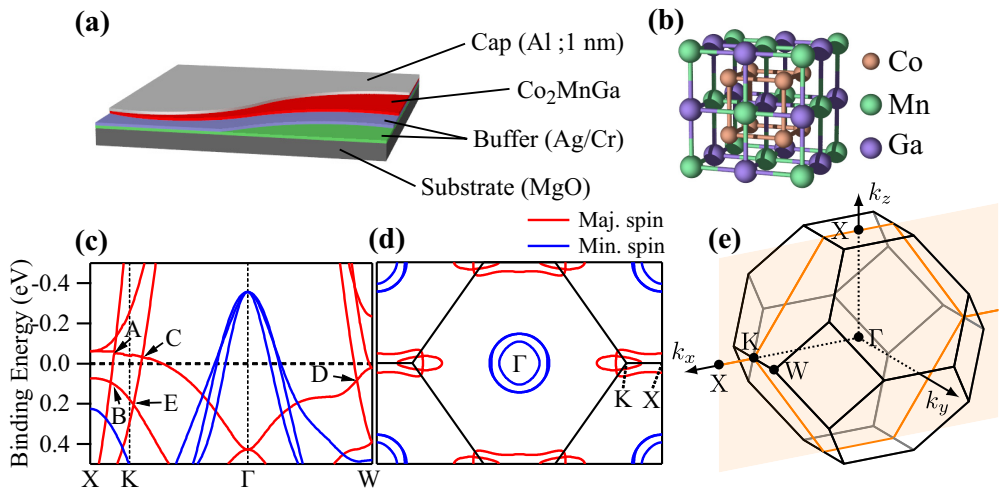

FIG. 1. (a) Cross-sectional view of Co_2MnGa film on MgO substrate with Ag/Cr buffer layers and Al capping layer. (b) Crystal structure of Co_2MnGa. (c), (d) Calculated bulk band structures along X-K-Γ-W line and cross sectional Fermi surface on k_x-k_z plane. Majority- and minority-spin bands are denoted in red and blue solid lines, respectively. (e) Bulk Brillouin zone with a plane corresponding to panel (d).

energy [32]. ARPES utilizing vacuum ultraviolet (VUV) synchrotron radiation for bulk single-crystal [15] and thin-film [7] Co_2MnGa probed the Weyl nodes that accompany the large magnetic flux (Berry curvature). The latter work on the permanently magnetized film uncovered the spin characteristics and claimed that the Weyl cones were created in the majority-spin channel, with the crossing points near the Fermi level. However, because of the poor out-of-plane momentum resolution, the three-dimensional Fermi surface information, needed to understand the detailed transport phenomena, was masked. The Heusler-type alloys generally have strong k_z energy-band dispersions arising from the three-dimensional nature of their crystal structures. Hence, ARPES utilizing synchrotron radiation in the soft x-ray region (400–1000 eV) would be ideal because it can reveal the bulk band structures in three dimensions. In the "universal curve" of inelastic mean free path vs kinetic energy for outgoing photoelectrons, the path is largely elongated to 2 nm, which is linked to the improved surface-perpendicular momentum resolution. Furthermore, free-electron parabolas become a better approximation to describe the photoelectron final states, and they simplify the matrix element incorporated in Fermi's golden rule for photoelectron emission. Hard x-ray photoelectron spectroscopy is expected to be the most bulk-sensitive and has played a significant role in investigating the bulk density of states. In the only known report on the k-resolved hard x-ray photoelectron spectroscopy for a Co_2MnGa thin film, the overall band structures were observed, but the Weyl crossing features were not resolved [32]. This may have been because of inherently poor momentum resolution and/or an enhanced Debye-Waller factor that would broaden ARPES features. Recently, three-dimensional bulk band structures of *in situ* cleaved Co_2MnGe single crystals have been acquired via soft x-ray ARPES, where the electron number is larger by one, per formula unit, than that of Co_2MnGa [16]. Hence, we have used the same technique to examine the three-dimensional bulk Fermi surfaces and band structures of Co_2MnGa films beneath a capping layer.

II. EXPERIMENTAL

Thin-film Co_2MnGa was prepared via the magnetron sputtering method at the National Institute for Materials Science (Tsukuba, Japan). A 30-nm-thick Co_2MnGa film was grown via Ar^+ ion sputtering of a Co_2MnGa-alloy target onto a MgO substrate, with buffer layers of Cr (10 nm) and Ag (100 nm) to obtain atomically flat surfaces, as in giant magnetoresistive devices [33,34]. The Co_2MnGa film was deposited at an ambient temperature and annealed *in situ* at 550 °C to induce atomic order. It was capped with a 1-nm Al layer to prevent further surface oxidation. The film structure is schematically shown in Fig. 1(a). X-ray diffraction measurement confirmed the (001)-oriented epitaxial growth and almost perfect $L2_1$ ordered phase of the film [see Fig. 1(b)] as described in the Supplemental Material [35], and the atomic composition was determined by x-ray fluorescence measurement to be 47.0 at. % Co, 25.6 at. % Mn, and 27.4 at. % Ga, for a valence electron number of 27.4. Single-crystalline bulk samples of Co_2MnGe were grown by the Bridgman method, where the mother polycrystalline ingot of about 20 g weight was heated up to 1362 K and then an alumina crucible was pulled down with the rate of 5 mm/hour. After confirming the crystal orientation by Laue's back reflection method, the crystals were cut into stripes in the direction parallel to ⟨100⟩ from the (110) disk. The $L2_1$ ordering was also confirmed by the Laue diffraction spots [35].

Soft x-ray ARPES was performed at BL25SU of SPring-8 (Sayo, Japan) [36]. A circularly polarized synchrotron radiation beam was used to observe the maximum number of bands. The penetration depth of photoelectrons in the kinetic energy region for this work (430 eV to 630 eV) was as large as 20 Å [37]. The spot size was about 10 μm × 10 μm, and the energy and angular resolutions were <80 meV and <0.2°, respectively. The sample temperature was 40 K for all the measurements, and the analyzer slit was along the k_x axis, which was parallel to the Co_2MnGa [110] axis.

First-principles density-functional calculations were performed with the WIEN2k program [38], using the spin-polarized generalized-gradient approximation [39]. The muffin-tin approximation was adopted for the potential; the muffin-tin radius R_{MT} of each atom was $R_{\mathrm{MT}}^{\mathrm{Co}} = R_{\mathrm{MT}}^{\mathrm{Mn}} = 2.32$ bohrs and $R_{\mathrm{MT}}^{\mathrm{Ga}} = 2.26$ bohrs. The wave functions were expanded into spherical harmonics with integer ℓ ranging up to $\ell_{\max} = 10$ in the muffin-tin spheres, and by plane waves in the interstitial region with a cutoff of $R_{\mathrm{MT}}^{\mathrm{Ga}} K_{\max} = 7$. The Fourier charge density was expanded up to $G_{\max} = 12$ bohr^{-1}. The k space was divided into a uniform $21 \times 21 \times 21$ mesh. The $RK_{\max}$, $\ell_{\max}$, $G_{\max}$, and k points were sufficient to stabilize the shape of the density of states. The lattice constants were set to $a = b = c = 5.755$ Å (estimated experimental values) and $\alpha = \beta = \gamma = 90^{\circ}$, and the $L2_1$ ($Fm\bar{3}m$) phase had atomic positions of Co (0.25, 0.25, 0.25), Mn (0, 0, 0), and Ga (0.5, 0.5, 0.5). Because previous studies indicated that the on-site Coulomb interaction U played a minor role [40,41], it was not considered here.

III. RESULTS AND DISCUSSION

In Fig. 1(c) are shown calculated band structures along the X-K-Γ-W line in the bulk Brillouin zone. In addition to downward dispersions crossing the Fermi level E_{F} in the minority-spin channel near the Γ point, some intercrossing Weyl cones were found near the K and W points in the majority-spin channel, with crossing points labeled A, B, C, D, and E in Fig. 1(c). These Weyl cones were tilted, where one band had a steep dispersion while the other was flat. Some of these Weyl cones were reported to be responsible for the high ANE and AHE [7]. Calculated Fermi surfaces are mapped in Fig. 1(d) on the k_x-k_z plane, involving the Γ, X, and K points depicted in Fig. 1(e). A double (or triple, to be precise) circular-shaped Fermi surface in the minority-spin channel surrounded the Γ point. This was related to the minority-spin downward dispersion mentioned above. An anisotropic Fermi surface elongated along the X-K line was found around the X point in the majority-spin channel, as shown in Fig. 1(d).

Experimental constant-energy contours mapped on the k_x-k_z plane were obtained by sequentially changing the incident photon energies. Elliptical Fermi pockets were centered at $(k_x, k_z) = (-3.1, 11)$ Å^{-1}, $(0, 11)$ Å^{-1}, and $(-1.5, 12)$ Å^{-1}, as marked with arrows α in Fig. 2. With increasing binding energy E_{B}, the size of the pocket α increased. The photoelectron intensity distributions for the equivalent hole pockets enclosing the Γ points were found to vary depending on its location in k space. For instance, the intensity distribution around $k_x = 0$ Å^{-1} was different from that near $k_x = -3$ Å^{-1} as shown in Figs. 2(a)–2(f). It was ascribed to the matrix element effect of the photoelectron emission process with a fixed light polarization along k_x as typically seen in d-orbital compounds [42]. Another feature was β, which appeared near $(k_x, k_z) = (\pm 0.5, 12)$ Å^{-1} at $E_{\mathrm{B}} = 0$ eV, and moved toward the Γ point as E_{B} increased. Finally, β merged with α at $E_{\mathrm{B}} = 0.25$ eV [Fig. 2(f)]. The observed features α and β were roughly reproduced by calculated isoenergy surfaces, indicated by red and blue solid lines in Fig. 2. This result demonstrated the energy dispersion of the bulk bands along the out-of-plane momentum axis, even in the presence of a capping layer, because of the improved k_z resolution ($\delta k_z \sim 0.05$ Å^{-1}) and photoelectron penetration depth (λ) ~ 20 Å of soft x-ray ARPES as compared to those of VUV-ARPES ($\delta k_z \sim 0.5$ Å^{-1}, $\lambda \sim 5$ Å). The Fermi surfaces mapped on the k_x-k_y plane, acquired at 455-eV and 552-eV excitations, are shown in Figs. 2(i), 2(j) respectively. Fourfold-symmetric features reflecting the (001) surface symmetry are recognized for both excitation energies. The shape of the Fermi surface was sensitive to the incident photon energy. At 455-eV excitation [Fig. 2(i)], a circular-shaped Fermi surface was observed in the center, which corresponded to the feature α on the k_x-k_z plane [Fig. 2(a)]. At 552-eV excitation [Fig. 2(j)], a diamond-shaped Fermi surface was observed in the center, and the feature α was again observed in the second Brillouin zone. When the experimental results were compared with the calculated band structures in Figs. 2(i), 2(j) feature α was created in the minority-spin channel and the diamond-shaped feature in the majority-spin channel.

Figures 2(k)–2(m) show the ARPES results taken at 660-eV, 552-eV, and 455-eV excitations, respectively, so that the energy dispersions can be approximately visualized along the high-symmetry lines. At 455-eV and 660-eV excitations [Figs. 2(k), 2(m)], symmetric holelike bands were observed near the zone center ($k_x = 0$ Å^{-1}). These corresponded to feature α [Figs. 2(a), 2(i)], and indicated a downward dispersion with a convex top above E_{F}. The band α near E_{F} was more clearly identified with the 455-eV excitation than with the 660-eV excitation, and was also recognized around $k_x = -3.1$ Å^{-1} (next Γ point). In addition, the E_{F} crossing features (β) were found at 552-eV excitation, and merged with the bands α around $E_{\mathrm{B}} = 0.25$ eV. The ARPES results at 455-eV and 660-eV excitations were expected to trace the same high-symmetry lines. A holelike band near $k_x = 0$ Å^{-1} was commonly seen in both cases. Another common feature was a downward dispersion with an energy maximum approximately at $E_{\mathrm{B}} = 0.24$ eV around $k_x = \pm 1.5$ Å^{-1}. At 660-eV excitation, there were multiple bands with an upward dispersion around $k_x = \pm 1.5$ Å^{-1} [Fig. 2(k)], while there was no significant intensity in the corresponding region at 455-eV excitation [Fig. 2(m)]. The difference in the photoelectron intensities at these two photon energies was because of the photoelectron-transition-probability matrix elements.

To discuss the band structures along the Γ-K-X line, the ARPES images along the in-plane k_x lines at $k_z/(4\pi/a) = 6.0$ and 5.5 [see Fig. 3(t)] were extracted and depicted in Figs. 3(a), 3(b) respectively. In Fig. 3(b), $k_{\Gamma\mathrm{K}} = 1.54$ Å^{-1} corresponds to the photoelectrons emitted perpendicular to the sample surface plane. For $k_x > 0$ Å^{-1}, the photoelectron intensity was normalized by the areal intensity of momentum distribution curves, as shown in the right panel of Fig. 3(a). In Figs. 3(a), 3(b) the photoelectron intensity peaks are marked by open circles and squares and symmetrized along with the Brillouin zone symmetry. For the band structures in the energy region $E_{\mathrm{B}} > 0.2$ eV, an upwardly convex parabolic band with a vertex at $E_{\mathrm{B}} \sim 0.65$ eV was observed near $k_{\Gamma\mathrm{K}} = 0$ Å^{-1} (Γ point), as shown in Fig. 3(a). A parabolic band with a vertex at $E_{\mathrm{B}} \sim 0.25$ eV can also be seen near the X point in Fig. 3(a), and the intensity near the vertex was also recognized in Fig. 3(b). These experimentally observed bands were

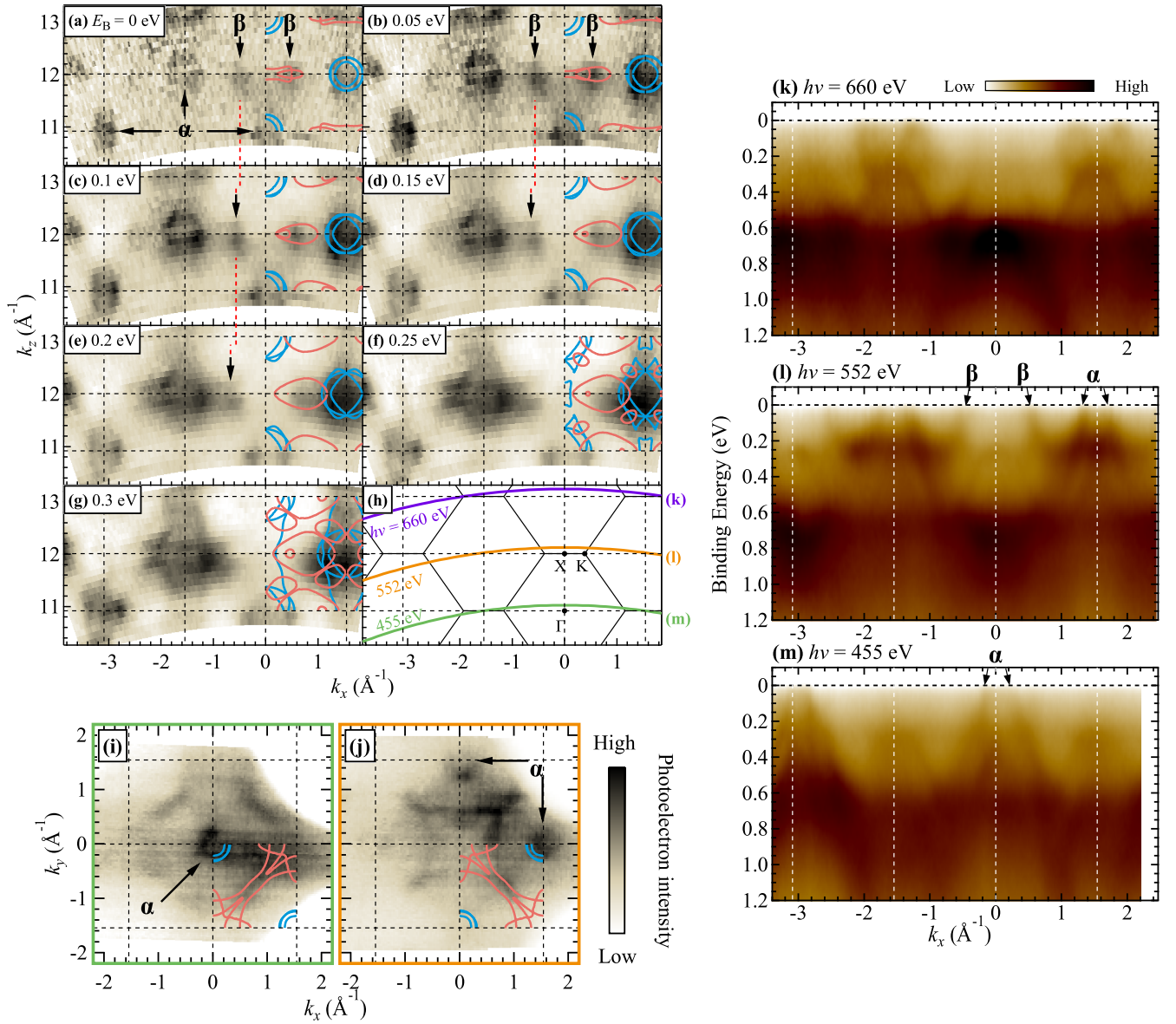

FIG. 2. (a)–(g) Constant-energy surface on k_x-k_z plane at $E_B = 0, 0.05, 0.1, \ldots, 0.3$ eV, respectively. Calculated results are also shown with the color of red (majority-spin components) and blue (minority). (h) Brillouin zone boundary and high-symmetry points on k_x-k_z plane are shown on the same scale as the panels (a)–(g). (i), (j) Fermi surfaces taken at photon energy of $h\nu = 455$ and 552 eV. Calculated results at $k_z = 0$ Å^{-1} and $k_z = 2\pi/a$ Å^{-1} are superimposed. (k)–(m) ARPES results at $h\nu = 660, 552, 455$ eV, respectively. Dashed lines are drawn every $2\sqrt{2}\pi/5.755$, which approximately corresponds to the Γ-K-X of the Brillouin zone.

well reproduced in the first-principles calculations. Furthermore, a downwardly convex parabolic band with a vertex at $E_B \sim 0.8$ eV was observed at the X point [Fig. 3(b)]. Those experimental features were in an excellent agreement with the calculated band structures shown in Fig. 3(c) when we considered a 0.2 eV downward shift in the theoretical dispersions. Those observed band structures corresponded to the majority-spin parabolic bands.

For band structures near E_F, in addition to the α and β bands, a parabolic band with an upward dispersion was observed with a vertex near $E_B = 0.3$ eV along the K-X-K line, as shown in Fig. 3(a). The momentum distribution curve of this band at E_F [see cut (a) in Fig. 3(t)] is shown in Fig. 3(d). In addition to two peaks for the hole pocket enclosing the Γ point, there were at least two components at every K point, indicating the presence of two bands that cross E_F. The ARPES images at various k_z lines and their second derivatives, where the band β was observed, are shown in Figs. 3(e)–3(i) and Figs. 3(j)–3(n), respectively. The calculated band dispersions along the corresponding momenta are also shown in Figs. 3(o)–3(s). The band β extracted from Fig. 3(b) was overlaid in panels (g), (l) (squares). A steep band dispersion γ crossing E_F was observed around $k_{\Gamma K} = -1.1$ Å^{-1} that was near the K point, as shown in Figs. 3(g), 3(l). This indicated that the γ band corresponded to the majority-spin band, shown by the first-principles thick red line [Fig. 3(q)]. In the evolution of the ARPES images along the k_z line [Figs. 3(e)–3(i)], the photoelectron intensity of the band γ diminished when it departed from the K point [Figs. 3(f), 3(h)], and was completely lost

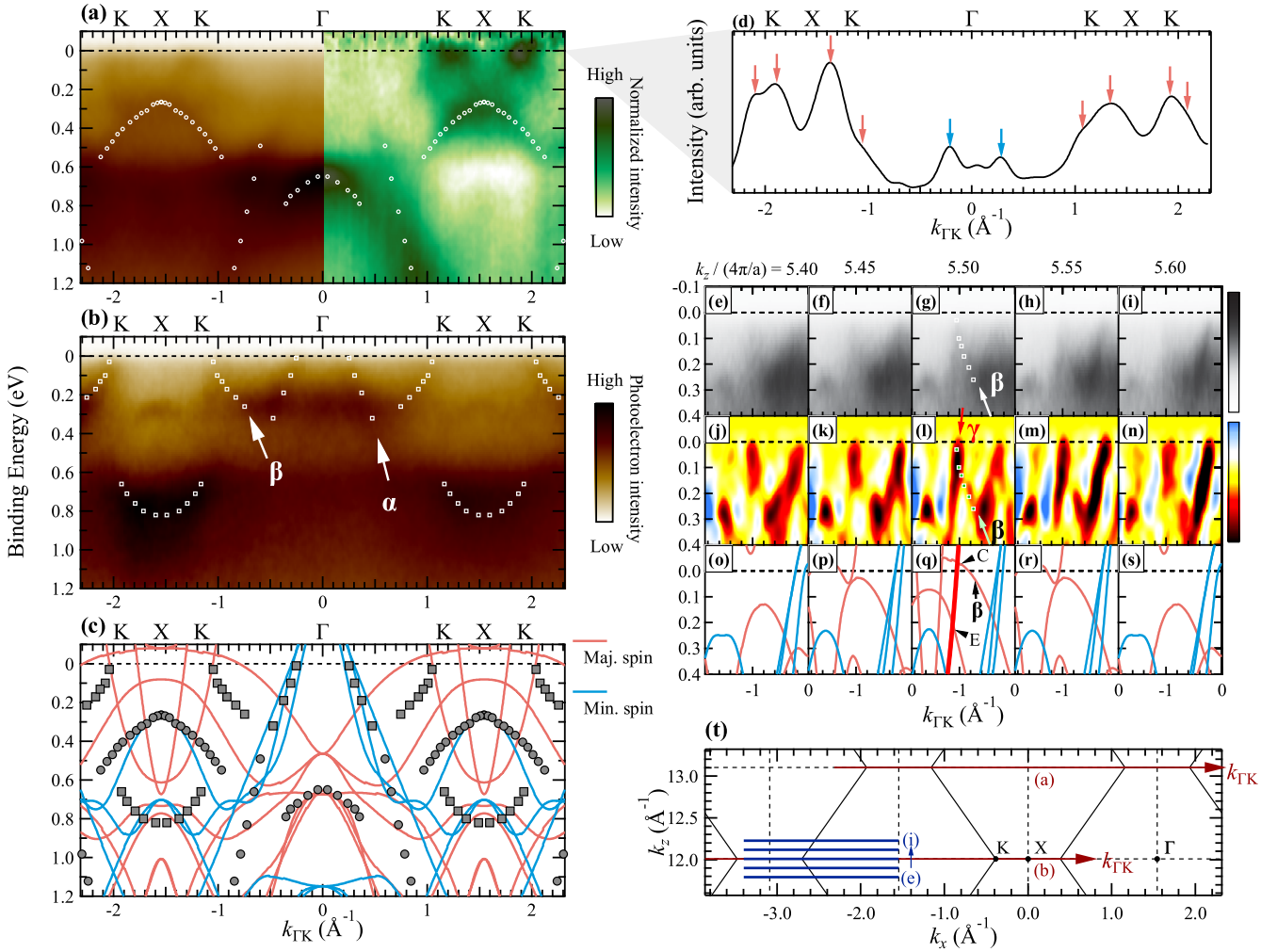

FIG. 3. (a), (b) ARPES images at $k_z/(4\pi/a) = 6.0, 5.5$, respectively. The $k_{\Gamma K} = 0$ Å^{-1} corresponds to $k_x = 0$ Å^{-1} and $k_x = -1.5$ Å^{-1}, respectively. A guide to the band structure visualized from the photoelectron intensity is shown in white marker. For panel (a), the intensity in the $k_x > 0$ Å^{-1} region is normalized in the energy direction using the area intensity of the momentum distribution curves. (c) Calculated band dispersion through Γ-K-X (solid line) and the band structure estimated in panels (a) and (b) are overlaid. (d) Momentum distribution curve along the cut (a) in panel (t). (e)–(i) ARPES images around K point. (j)–(n) Second derivative of ARPES images corresponding to panels (e)–(i). (o)–(s) Calculated band dispersions corresponding to panels (e)–(i). (t) Brillouin zone boundaries on k_x-k_z plane and momentum path of other panels.

when it moved farther away, as shown in Figs. 3(e), 3(i). Furthermore, the band γ intersects the band β at $k_{\Gamma K} = -1.1$ Å^{-1}. These features were reproduced by the calculations [Fig. 3(q)] when the theoretical E_F was shifted upward by 0.2 eV to coincide with the crossing point. This confirmed that the band crossing observed for the Co_2MnGa sample, with the valence electron number $N_V = 27.4$, corresponded to the crossing C in Fig. 1(c). According to a previous report, AHE and ANE increase with increasing N_V, and thus are higher when $N_V = 28.5$ [7]. The Fermi level was quite close to the point A, which was energetically higher than point C [see Fig. 1(c)] for the sample with $N_V = 28.5$. This was consistent with the experimental result that the transverse Hall and thermoelectric conductivities of the sample with $N_V = 27.3$ were about 70% of those for the electron-doped sample with $N_V = 28.5$. It was also in line with the fact that the anomalous Nernst thermopower reached 6.2 μV/K [7], which was the highest in thin films [43,44]. In the previous report, the observed Weyl crossing of the sample with $N_V = 27.3$ coincided with another crossing (E) that was the farthest from E_F of the five crossings in Fig. 1(c). However, the size of the hole Fermi surface surrounding the Γ point was similar to the present case. The higher bulk sensitivity and the improved k_z resolution enabled us to revise the conclusion that the Weyl crossing of the sample with $N_V = 27.3$ (27.4) corresponded to the crossing C in Fig. 1(c).

Finally, we compared the observed Fermi surfaces and band structures of the Co_2MnGa thin film with those of the Co_2MnGe bulk crystal that were previously reported and experimentally shown via soft x-ray ARPES to have a half-metallic band structure [16]. One valence electron per formula unit is added when Ga is replaced with Ge. Reflecting the half-metallic band structure, where only the majority-spin bands cross E_F, the observed Fermi surface shapes of Co_2MnGe mapped on the plane [Fig. 4(j)] were completely different from those of Co_2MnGa [Figs. 4(a), 4(c)]. However, the

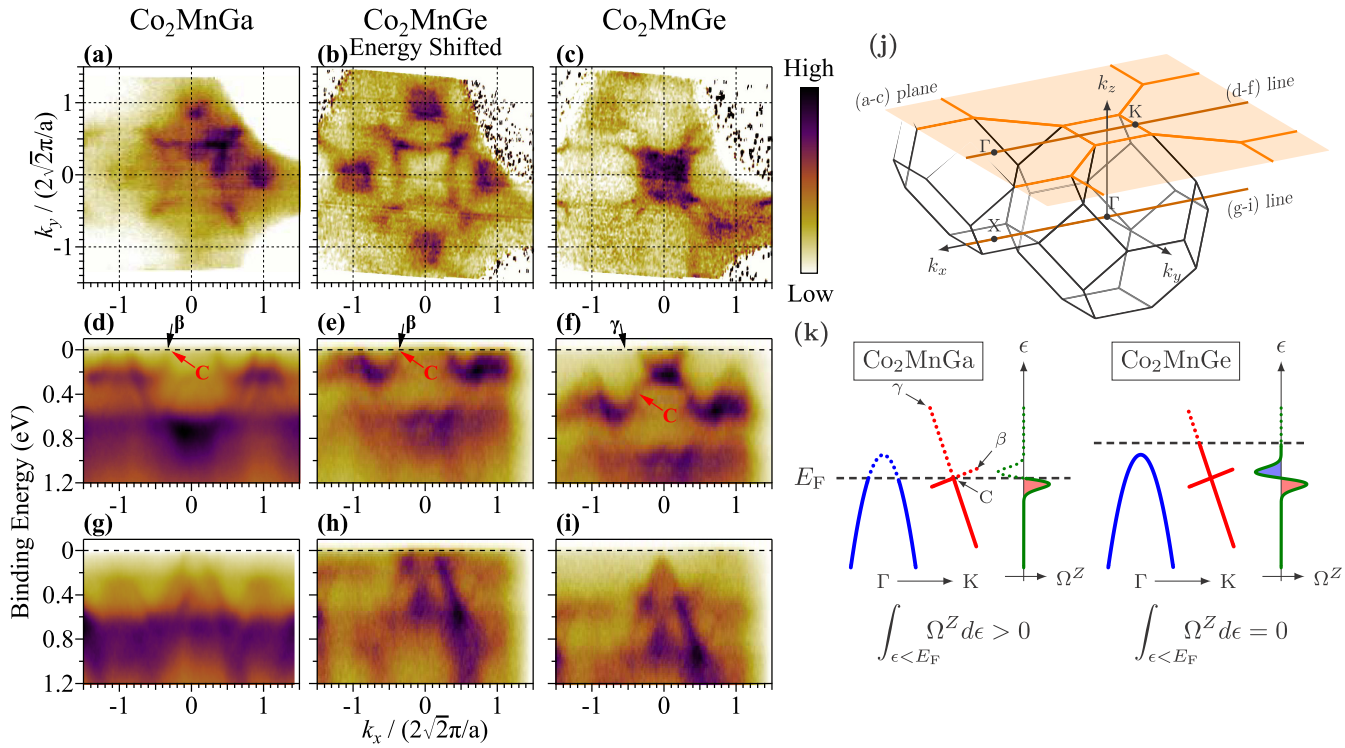

FIG. 4. (a) Fermi surface maps in the k_x-k_y plane acquired by ARPES for Co_2MnGa. (b), (c) Energy-shifted and original Fermi surfaces for Co_2MnGe, respectively. (d), (g) ARPES energy dispersions of Co_2MnGa along the line at $k_z/(4\pi/a) = 5.5$ and $k_z/(4\pi/a) = 5.0$, respectively. (e), (h) Energy-shifted ARPES energy dispersions of Co_2MnGe along the line at $k_z/(4\pi/a) = 5.5$ and $k_z/(4\pi/a) = 5.0$, respectively. (f), (i) Original ARPES energy dispersions of Co_2MnGe along the line at $k_z/(4\pi/a) = 5.5$ and $k_z/(4\pi/a) = 5.0$, respectively. (j) A plane for Fermi surface maps in panels (a)–(c) and lines for energy dispersions in panels (d)–(f) and (g)–(i). (k) Schematics of hole pockets and tilted Weyl cones with Berry curvatures.

constant-energy contour of Co_2MnGe sliced at $E_B = 0.4$ eV resembled the Fermi surface of Co_2MnGa [Figs. 4(a), 4(b)]. The energy dispersions along the lines at $k_z/(4\pi/a) = 5.5$ and $k_z/(4\pi/a) = 5.0$ [Fig. 4(j)] of Co_2MnGe that were artificially shifted by 0.4 eV [Figs. 4(e), 4(h)] were in excellent agreement with those of Co_2MnGa [Figs. 4(d), 4(g)], which indicated that a rigid band picture could be applicable to both Co_2MnGa and Co_2MnGe. It also reconfirmed that all the features observed in the Co_2MnGa films were of bulk origin. A consequence was that the crossing C was adjusted at E_F by rigidly shifting the entire band structures of Co_2MnGe by 0.4 eV. As schematically shown in Fig. 4(k), anomalous Hall and Nernst conductivities are enhanced when the crossing point is placed at or near E_F as in the case of Co_2MnGa, while they become low if the crossing point is far below E_F because the anomalous Hall conductivity is described with a sum of Berry curvature over all occupied bands [45]. Therefore, fine carrier tuning was required to maximize the AHE and ANE efficiencies [7]. The present study showed that this could be realized by replacing Ga with Ge, so that the Weyl crossings matched E_F.

The experimental dispersion of the band β was much steeper than the calculations [see Figs. 3(l), 3(q)]. The VUV-ARPES exhibited similar behavior [7]. This discrepancy might have been attributed to an electron correlation effect not considered in the first-principles calculations. Hence, experimental observations of bulk band structures are crucial, because the slope of the energy dispersion might affect the magnitude of the Berry curvature and thus modify the Nernst thermopower.

IV. CONCLUSION

We performed soft x-ray ARPES on a Co_2MnGa thin film protected with a 1-nm Al capping layer and observed band dispersions in the absence of an *in situ* surface treatment. The periodicity of the observed ARPES intensity variations coincided with its in-plane and out-of-plane Brillouin zone boundaries estimated from experimental lattice parameters. This reflected the bulk band structures of the sample without effects from the capping layer. Near the Γ point, we found an upwardly convex minority-spin parabolic band that crossed E_F, indicating that Co_2MnGa had a non-half-metal band structure, in contrast to Co_2MnGe. The intersecting linear dispersion had a crossing point near E_F, which was understood in terms of the Weyl cone in the majority-spin channel. We thus concluded that the observed Weyl cone was of bulk origin and was responsible for the very large anomalous Nernst and Hall effects. A close comparison of Co_2MnGa and Co_2MnGe isoenergy surfaces verified the validity of the rigid-band picture, indicating that fine carrier tuning was possible by replacing Ga with Ge to maximize the anomalous Hall and Nernst conductivities. ARPES via soft x-ray synchrotron radiation is thus a powerful way to

study three-dimensional bulk band structures, as well as Fermi surfaces, for the *ex situ* grown films that exhibit various functionalities, even in the presence of protected layers. Overall, this work widens research in energy band structures for the purpose of upgrading the functionalities.

ACKNOWLEDGMENTS

This work was financially supported by JSPS KAKENHI (Grants No. 17H06152, No. 17H06138, No. 18H01690, No. 18H03683, and No. 21K14540), and partially supported by PRESTO Scientific Innovation for Energy Harvesting Technology (No. JPMJPR17R5) from JST, Japan. The soft x-ray ARPES experiments were performed with the approval of Japan Synchrotron Radiation Research Institute (Proposals No. 2018B1465 and No. 2019A1548). Micro-ARPES instruments were developed by the Photon and Quantum Basic Research Coordinated Development Program from MEXT. T.Y. was financially supported by Grant-in-Aid for JSPS Fellows No. 18J22309.

[1] A. Sakai, Y. P. Mizuta, A. A. Nugroho, R. Sihombing, T. Koretsune, M.-T. Suzuki, N. Takemori, R. Ishii, D. Nishio-Hamane, R. Arita, P. Goswami, and S. Nakatsuji, Nat. Phys. **14**, 1119 (2018).

[2] S. N. Guin, K. Manna, J. Noky, S. J. Watzman, C. Fu, N. Kumar, W. Schnelle, C. Shekhar, Y. Sun, J. Gooth, and C. Felser, NPG Asia Mater. **11**, 16 (2019).

[3] L. Xu, X. Li, L. Ding, T. Chen, A. Sakai, B. Fauqué, S. Nakatsuji, Z. Zhu, and K. Behnia, Phys. Rev. B **101**, 180404(R) (2020).

[4] D. Xiao, Y. Yao, Z. Fang, and Q. Niu, Phys. Rev. Lett. **97**, 026603 (2006).

[5] D. Xiao, M.-C. Chang, and Q. Niu, Rev. Mod. Phys. **82**, 1959 (2010).

[6] G. Chang, S.-Y. Xu, X. Zhou, S.-M. Huang, B. Singh, B. Wang, I. Belopolski, J. Yin, S. Zhang, A. Bansil, H. Lin, and M. Z. Hasan, Phys. Rev. Lett. **119**, 156401 (2017).

[7] K. Sumida, Y. Sakuraba, K. Masuda, T. Kono, M. Kakoki, K. Goto, W. Zhou, K. Miyamoto, Y. Miura, T. Okuda, and A. Kimura, Commun. Mater. **1**, 89 (2020).

[8] K.-i. Uchida, W. Zhou, and Y. Sakuraba, Appl. Phys. Lett. **118**, 140504 (2021).

[9] W. Zhou, K. Yamamoto, A. Miura, R. Iguchi, Y. Miura, K.-i. Uchida, and Y. Sakuraba, Nat. Mater. **11**, 463 (2021).

[10] S. Hüfner, *Photoelectron Spectroscopy: Principles and Applications*, 3rd ed. (Springer, Berlin, 2003).

[11] B. Balke, G. H. Fecher, H. C. Kandpal, C. Felser, K. Kobayashi, E. Ikenaga, J.-J. Kim, and S. Ueda, Phys. Rev. B **74**, 104405 (2006).

[12] K. Miyamoto, A. Kimura, Y. Miura, M. Shirai, M. Ye, Y. Cui, K. Shimada, H. Namatame, M. Taniguchi, Y. Takeda, Y. Saitoh, E. Ikenaga, S. Ueda, K. Kobayashi, and T. Kanomata, Phys. Rev. B **79**, 100405(R) (2009).

[13] S. Ouardi, G. H. Fecher, B. Balke, A. Beleanu, X. Kozina, G. Stryganyuk, C. Felser, W. Klöß, H. Schrader, F. Bernardi, J. Morais, E. Ikenaga, Y. Yamashita, S. Ueda, and K. Kobayashi, Phys. Rev. B **84**, 155122 (2011).

[14] V. Alijani, S. Ouardi, G. H. Fecher, J. Winterlik, S. S. Naghavi, X. Kozina, G. Stryganyuk, C. Felser, E. Ikenaga, Y. Yamashita, S. Ueda, and K. Kobayashi, Phys. Rev. B **84**, 224416 (2011).

[15] I. Belopolski, K. Manna, D. S. Sanchez, G. Chang, B. Ernst, J. Yin, S. S. Zhang, T. Cochran, N. Shumiya, H. Zheng, B. Singh, G. Bian, D. Multer, M. Litskevich, X. Zhou, S.-M. Huang, B. Wang, T.-R. Chang, S.-Y. Xu, A. Bansil *et al.*, Science **365**, 1278 (2019).

[16] T. Kono, M. Kakoki, T. Yoshikawa, X. Wang, K. Goto, T. Muro, R. Y. Umetsu, and A. Kimura, Phys. Rev. Lett. **125**, 216403 (2020).

[17] W. H. Wang, M. Przybylski, W. Kuch, L. I. Chelaru, J. Wang, Y. F. Lu, J. Barthel, H. L. Meyerheim, and J. Kirschner, Phys. Rev. B **71**, 144416 (2005).

[18] G. H. Fecher, B. Balke, A. Gloskowskii, S. Ouardi, C. Felser, T. Ishikawa, M. Yamamoto, Y. Yamashita, H. Yoshikawa, S. Ueda, and K. Kobayashi, Appl. Phys. Lett. **92**, 193513 (2008).

[19] O. Gaier, J. Hamrle, B. Hillebrands, M. Kallmayer, P. Pörsch, G. Schönhense, H. J. Elmers, J. Fassbender, A. Gloskovskii, C. A. Jenkins, C. Felser, E. Ikenaga, Y. Sakuraba, S. Tsunegi, M. Oogane, and Y. Ando, Appl. Phys. Lett. **94**, 152508 (2009).

[20] M. Hahn, G. Schönhense, E. A. Jorge, and M. Jourdan, Appl. Phys. Lett. **98**, 232503 (2011).

[21] J.-P. Wüstenberg, R. Fetzer, M. Aeschlimann, M. Cinchetti, J. Minár, J. Braun, H. Ebert, T. Ishikawa, T. Uemura, and M. Yamamoto, Phys. Rev. B **85**, 064407 (2012).

[22] M. Kolbe, S. Chadov, E. A. Jorge, G. Schönhense, C. Felser, H.-J. Elmers, M. Kläui, and M. Jourdan, Phys. Rev. B **86**, 024422 (2012).

[23] R. Fetzer, J.-P. Wüstenberg, T. Taira, T. Uemura, M. Yamamoto, M. Aeschlimann, and M. Cinchetti, Phys. Rev. B **87**, 184418 (2013).

[24] M. Jourdan, J. Minár, J. Braun, A. Kronenberg, S. Chadov, B. Balke, A. Gloskovskii, M. Kolbe, H. J. Elmers, G. Schönhense, H. Ebert, C. Felser, and M. Kläui, Nat. Commun. **5**, 3974 (2014).

[25] X. Kozina, J. Karel, S. Ouardi, S. Chadov, G. H. Fecher, C. Felser, G. Stryganyuk, B. Balke, T. Ishikawa, T. Uemura, M. Yamamoto, E. Ikenaga, S. Ueda, and K. Kobayashi, Phys. Rev. B **89**, 125116 (2014).

[26] J. Braun, M. Jourdan, A. Kronenberg, S. Chadov, B. Balke, M. Kolbe, A. Gloskovskii, H. J. Elmers, G. Schönhense, C. Felser, M. Kläui, H. Ebert, and J. Minár, Phys. Rev. B **91**, 195128 (2015).

[27] S. Andrieu, A. Neggache, T. Hauet, T. Devolder, A. Hallal, M. Chshiev, A. M. Bataille, P. Le Fèvre, and F. Bertran, Phys. Rev. B **93**, 094417 (2016).

[28] C. Guillemard, S. Petit-Watelot, L. Pasquier, D. Pierre, J. Ghanbaja, J.-C. Rojas-Sánchez, A. Bataille, J. Rault, P. Le Fèvre, F. Bertran, and S. Andrieu, Phys. Rev. Appl. **11**, 064009 (2019).

[29] C. Lidig, J. Minár, J. Braun, H. Ebert, A. Gloskovskii, J. A. Krieger, V. Strocov, M. Kläui, and M. Jourdan, Phys. Rev. B **99**, 174432 (2019).

[30] T. Kono, M. Kakoki, T. Yoshikawa, X. Wang, K. Sumida, K. Miyamoto, T. Muro, Y. Takeda, Y. Saitoh, K. Goto, Y. Sakuraba, K. Hono, and A. Kimura, Phys. Rev. B **100**, 165120 (2019).

[31] C. Guillemard, W. Zhang, G. Malinowski, C. de Melo, J. Gorchon, S. Petit-Watelot, J. Ghanbaja, S. Mangin, P. Le Févre, F. Bertran, and S. Andrieu, Adv. Mater. **32**, 1908357 (2020).

[32] S. Chernov, C. Lidig, O. Fedchenko, K. Medjanik, S. Babenkov, D. Vasilyev, M. Jourdan, G. Schönhense, and H. J. Elmers, Phys. Rev. B **103**, 054407 (2021).

[33] J. W. Jung, Y. Sakuraba, T. T. Sasaki, Y. Miura, and K. Hono, Appl. Phys. Lett. **108**, 102408 (2016).

[34] B. Büker, J. Jung, T. Sasaki, Y. Sakuraba, Y. Miura, T. Nakatani, A. Hütten, and K. Hono, Phys. Rev. B **103**, L140405 (2021).

[35] See Supplemental Material at http://link.aps.org/supplemental/10.1103/PhysRevB.104.195112 for x-ray diffraction patterns of Co_2MnGa film, sample preparation procedures, and Laue diffraction patterns of Co_2MnGe single crystals.

[36] T. Muro, Y. Senba, H. Ohashi, T. Ohkochi, T. Matsushita, T. Kinoshita, and S. Shin, J. Synchrotron Radiat. **28**, 1631 (2021).

[37] S. Tanuma, C. J. Powell, and D. R. Penn, Surf. Interface Anal. **43**, 689 (2011).

[38] P. Blaha, K. Schwarz, G. K. H. Madsen, D. Kvasnicka, and J. Luitz, *WIEN2k, An Augmented Plane Wave + Local Orbitals Program for Calculating Crystal Properties* (Karlheinz Schwarz, Techn. Universität Wien, Austria, 2001).

[39] J. P. Perdew, K. Burke, and M. Ernzerhof, Phys. Rev. Lett. **77**, 3865 (1996).

[40] C. Tsirogiannis and I. Galanakis, J. Magn. Magn. Mater. **393**, 297 (2015).

[41] S. Sharma and S. K. Pandey, J. Magn. Magn. Mater. **403**, 1 (2016).

[42] V. Brouet, M. F. Jensen, P.-H. Lin, A. Taleb-Ibrahimi, P. Le Fèvre, F. Bertran, C.-H. Lin, W. Ku, A. Forget, and D. Colson, Phys. Rev. B **86**, 075123 (2012).

[43] H. Reichlova, R. Schlitz, S. Beckert, P. Swekis, A. Markou, Y.-C. Chen, D. Kriegner, S. Fabretti, G. Hyeon Park, A. Niemann, S. Sudheendra, A. Thomas, K. Nielsch, C. Felser, and S. T. B. Goennenwein, Appl. Phys. Lett. **113**, 212405 (2018).

[44] G.-H. Park, H. Reichlova, R. Schlitz, M. Lammel, A. Markou, P. Swekis, P. Ritzinger, D. Kriegner, J. Noky, J. Gayles, Y. Sun, C. Felser, K. Nielsch, S. T. B. Goennenwein, and A. Thomas, Phys. Rev. B **101**, 060406(R) (2020).

[45] Y. Yao, L. Kleinman, A. H. MacDonald, J. Sinova, T. Jungwirth, D.-s. Wang, E. Wang, and Q. Niu, Phys. Rev. Lett. **92**, 037204 (2004).